



LAWRENCE
LIVERMORE
NATIONAL
LABORATORY

Stability of finite difference discretizations of multi-physics interface conditions

B. Sjogreen, J. W. Banks

July 1, 2011

Communications in Computational Physics

Disclaimer

This document was prepared as an account of work sponsored by an agency of the United States government. Neither the United States government nor Lawrence Livermore National Security, LLC, nor any of their employees makes any warranty, expressed or implied, or assumes any legal liability or responsibility for the accuracy, completeness, or usefulness of any information, apparatus, product, or process disclosed, or represents that its use would not infringe privately owned rights. Reference herein to any specific commercial product, process, or service by trade name, trademark, manufacturer, or otherwise does not necessarily constitute or imply its endorsement, recommendation, or favoring by the United States government or Lawrence Livermore National Security, LLC. The views and opinions of authors expressed herein do not necessarily state or reflect those of the United States government or Lawrence Livermore National Security, LLC, and shall not be used for advertising or product endorsement purposes.

Stability of finite difference discretizations of multi-physics interface conditions

Björn Sjögreen* and Jeffrey W. Banks*

June 23, 2011

Abstract

We consider multi-physics computations where the Navier-Stokes equations of compressible fluid flow on some parts of the computational domain are coupled to the equations of elasticity on other parts of the computational domain. The different subdomains are separated by well-defined interfaces. We consider time accurate computations resolving all time scales. For such computations, explicit time stepping is very efficient. We address the issue of discrete interface conditions between the two domains of different physics that do not lead instability, or to a significant reduction of the stable time step size. Finding such interface conditions is non-trivial.

We discretize the problem with high order centered difference approximations, having summation by parts boundary closure. We derive L^2 stable interface conditions for the linearized one dimensional discretized problem. Furthermore, we generalize the interface conditions to the full non-linear equations, and demonstrate numerically their stable and accurate performance on a simple model problem. The energy stable interface conditions derived here through symmetrization of the equations contain the interface conditions derived through normal mode analysis by Banks and Sjögreen in [7] as a special case.

*Center for Applied Scientific Computing, L-422, LLNL, P.O. Box 808, Livermore, CA 94551, USA. This work performed under the auspices of the U.S. Department of Energy by Lawrence Livermore National Laboratory under Contract DE-AC52-07NA27344.

1 Introduction

This work will consider numerical simulation of multi-physics systems where two, or more, physics models are solved on different parts of a computational domain. These different multi-physics domains are assumed to be separated by well-defined interfaces. Interface coupling conditions, which couple the solutions in the various sub-domains, are defined on these well-defined boundaries.

In the literature, there is a large body of work relating to numerical treatment of this type of fluid-structure interface. By far the most common approach is to apply material motions from the solid domain as boundary conditions to the fluid while using the fluid stresses as boundary conditions on the solid. However, this approach can become problematic from a stability perspective for certain cases. As a result implicit, sometimes referred to as monolithic, approaches have often been adopted. Such schemes are effective, but introduce additional difficulties in terms of linear/nonlinear solvers and pre-conditioners.

Recent work in [7, 6] has shown that more symmetric approaches to interface condition imposition can result in favorable approximations, possibly with stability across all ranges of material parameters. The main purpose of the current work is to discuss the well-posedness of the continuous linearized fluid-structure problem and introduce a summation-by-parts discretization which mimics the energy behavior of the continuous operators. The operators which are thus derived have similar structure to those found in [7]. We will verify the accuracy of this new approach via manufactured solutions, and apply the schemes to a nontrivial problem of a Navier-Stokes fluid with an elastic-plastic solid.

The example studied here will be fluid/structure interaction in one space dimension, but the ideas are intended as more generally applicable. However, the techniques employed here have an impact on the choices available for extension to, for example, two space dimensions. This is an important point and so we provide here a brief discussion of these issues. The eventual numerical discretization of the governing equations and interface conditions investigated here requires a set of interface aligned grids. That is to say that the interface defining the boundary between two, or more, physics sub-domains must be represented in both computational sub-domains. This is shown graphically in Fig. 1. Here, the fluid equations are discretized on the blue grids and the solid is discretized on the red grid. The requirement

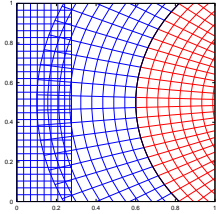


Figure 1: Graphic representation of possible computational setup in two space dimensions. Blue represents the fluid and red represents the solid.

that both computational sub-domains align with the material interface implies that other techniques are required to deal with external boundaries. In Fig. 1 we indicate that an overset grid approach [4] is used to treat the fluid domain, while a structured deforming grid is used for the solid. Other options are of course possible and include embedded boundaries, overset grids, unstructured grids, or others. The key requirement as it relates to this work is that the fluid and solid are discretized on grids which align to the material interface.

The remainder of this work is structured as follows. Section 2 describes the equations in full generality. In Section 3, we perform an energy estimate of the one dimensional continuous problem, and prove that the standard interface conditions lead to a well-posed problem with decreasing energy. Section 4 performs the same analysis for finite difference discretizations that satisfy the summation by parts principle. We find energy stable discretizations and give explicit formulas for the discrete interface conditions. Section 5 shows numerical examples in one space dimension. The method of manufactured solution is first used to verify the implementation and to study the numerical convergence order obtained for finite difference schemes of different formal accuracies. Finally, we simulate an elastic rod pulled by gravity into a compressible fluid. Conclusions are presented in Section 6.

2 Equations

Let the updated Lagrangian equations of motion,

$$\begin{aligned}
\rho J &= \rho_0 J_0 = m_0 \\
\rho \mathbf{u}_t &= -\nabla p + \operatorname{div} \sigma + \rho \mathbf{f} \\
\sigma_t &= -W\sigma - \sigma W^T + \lambda_e \operatorname{div} \mathbf{u} I + 2\mu_e D \\
\rho \epsilon_t &= -p \operatorname{div} \mathbf{u} + (\sigma : D) + \operatorname{div}(\kappa_e \nabla T) \\
\mathbf{x}_t &= \mathbf{u},
\end{aligned} \tag{1}$$

model the movement and deformation of an elastic-plastic body, see, e.g., [14]. The pressure, p , models plastic effects. The equations of structural mechanics for elastic materials, as described, e.g., in [2], are obtained from (1) by setting $p = 0$.

The density ρ , velocity \mathbf{u} , stress tensor σ , internal energy ϵ , and temperature T , are functions of (\mathbf{X}, t) . $\mathbf{X} = (X_1, X_2, X_3)$, the Lagrangian coordinates, which are the coordinates in a reference configuration at time zero. \mathbf{f} is a given, external, volume distributed forcing. The Eulerian coordinates

$$\mathbf{x} = \mathbf{x}(\mathbf{X}, t) \tag{2}$$

represent the position at time t of the material point that was located at \mathbf{X} at time zero. The partial derivative of a variable with respect to t with \mathbf{X} held fixed is here denoted by subscript t . In the continuum mechanics literature these material time derivatives are often instead denoted by D/Dt .

The derivative of (2) is denoted by

$$(F)_{i,j} = \frac{\partial x_i}{\partial X_j}$$

and its Jacobian by $J = \det(F)$. $m_0 = J_0 \rho_0$ denotes $J(X, 0) \rho(X, 0)$. The gradient, ∇ , and divergence operators act in the Eulerian coordinates, and can be evaluated in the Lagrangian frame by use of the coordinate mapping (2). I is the identity matrix, and the symmetric and skew-symmetric parts of the velocity gradient are defined as

$$D = \frac{1}{2}(\nabla \mathbf{u} + \nabla \mathbf{u}^T) \quad \text{and} \quad W = \frac{1}{2}(\nabla \mathbf{u} - \nabla \mathbf{u}^T).$$

The Lamé parameters μ_e and λ_e are in general functions of the spatial coordinate, and depend on the material. A thermodynamic relation $\epsilon = \epsilon(T)$

relates the temperature and internal energy. We will here use a linear relation $\epsilon = \alpha T$, where α is a given constant. The pressure, when present, is given through an equation of state, $p = p(\rho\epsilon, \rho)$.

The compressible Navier-Stokes equations,

$$\begin{aligned}\rho_t + \operatorname{div} \rho \mathbf{u} &= 0 \\ (\rho \mathbf{u})_t + \operatorname{div}(\rho \mathbf{u} \mathbf{u}^T + p \mathbf{I}) &= \operatorname{div}(\lambda \operatorname{div} \mathbf{u} \mathbf{I} + 2\mu D) + \rho \mathbf{f} \\ e_t + \operatorname{div}(\mathbf{u}(e + p)) &= \operatorname{div}(\lambda \mathbf{u} \operatorname{div} \mathbf{u} + 2\mu D \mathbf{u}) + \operatorname{div}(\kappa \nabla T)\end{aligned}\tag{3}$$

models the fluid. The pressure obeys the perfect gas law, $p = (\gamma - 1)(e - \rho|\mathbf{u}|^2/2)$, for a constant γ , where e is the total energy. The coefficients of viscosity are μ and λ , and κ is the heat conduction. λ is given by the zero bulk viscosity assumption $\lambda = -\frac{2}{3}\mu$. The equation of state $p = \rho T \frac{R}{M}$ is used to compute the temperature from the other variables. R is the universal gas constant, and M is the constant molar mass of the fluid. The variables in (3) are functions of the Eulerian variables (\mathbf{x}, t) . The notation for the density, velocity, and pressure, in the fluid is the same as used for the elastic material in (1). The superscripts (f) and (s) will denote variables in the fluid and solid respectively, but these superscripts are left out when the continuum type is clear from the context.

2.1 Interface conditions

The interface conditions at the fluid/solid boundary are the no-slip condition

$$\mathbf{u}^{(f)} = \mathbf{u}^{(s)},\tag{4}$$

normal stress continuity

$$-p^{(f)} \mathbf{n} + \lambda \operatorname{div} \mathbf{u}^{(f)} \mathbf{n} + 2\mu D^{(f)} \mathbf{n} = \sigma \mathbf{n} - p^{(s)} \mathbf{n},\tag{5}$$

and continuity of the temperature and of the heat flux

$$T^{(f)} = T^{(s)}\tag{6}$$

$$\kappa \frac{\partial T^{(f)}}{\partial n} = \kappa_e \frac{\partial T^{(s)}}{\partial n}.\tag{7}$$

\mathbf{n} is a unit vector normal to the interface, and $\partial/\partial n$ denotes the derivative in the direction \mathbf{n} in the Eulerian coordinate.

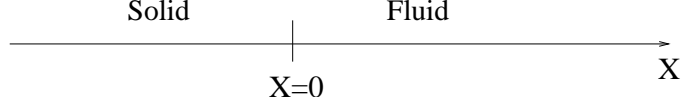


Figure 2: Domain for analysis of the one dimensional equations.

3 Energy estimate in one space dimension

The interface conditions (4)-(7) are natural conditions from physics considerations, and should therefore lead to a well-posed problem. In this section we prove that this is indeed the case. Furthermore, the analysis gives insight into how to construct stable finite difference discretizations.

Consider the one-dimensional domain outlined in Fig. 2, where an interface at the Eulerian coordinate $x_I(t)$ separates a fluid to the right and an elastic-plastic solid to the left. In Lagrangian coordinates, the interface is given by $X = 0$.

The equations (1), when restricted to one space dimension become

$$\begin{aligned}
 u_t &= \frac{1}{m_0}(\sigma - p)_X \\
 \sigma_t &= \frac{1}{x_X}(2\mu_e + \lambda_e)u_X \\
 m_0\epsilon_t &= (\sigma - p)u_X + \left(\frac{\kappa_e}{x_X}T_X\right)_X \\
 x_t &= u,
 \end{aligned} \tag{8}$$

for the domain $-\infty < X < 0$. Mass conservation in one dimension is $\rho x_X = m_0$, because $J = x_X$.

The fluid equations (3) are transformed to the coordinate X by the moving coordinate mapping $x = X + x_I(t)$, i.e., to a rigid frame that moves with the interface, and become

$$\begin{aligned}
 \rho_t + (\rho u - x'_I(t)\rho)_X &= 0 \\
 (\rho u)_t + (\rho u^2 + p - x'_I(t)\rho u)_X &= \frac{4}{3}\mu u_{XX} \\
 e_t + (u(e + p) - x'_I(t)e)_X &= \frac{4}{3}\mu(uu_X)_X + (\kappa T_X)_X
 \end{aligned} \tag{9}$$

on the domain $0 < X < \infty$.

3.1 Linearized problem

Linearize the Navier-Stokes system around a constant state $(\hat{\rho}, \hat{u}, \hat{T})$ with velocity $\hat{u} = -s$, where the constant velocity, s , is the linearized interface velocity $\hat{x}_I(t) = st$, to obtain

$$\begin{pmatrix} \rho \\ u \\ T \end{pmatrix}_t + \begin{pmatrix} 0 & \hat{\rho} & 0 \\ \frac{R}{M} \frac{\hat{T}}{\hat{\rho}} & 0 & \frac{R}{M} \\ 0 & (\gamma - 1)\hat{T} & 0 \end{pmatrix} \begin{pmatrix} \rho \\ u \\ T \end{pmatrix}_X = \frac{1}{\hat{\rho}} \begin{pmatrix} 0 \\ \frac{4}{3}(\mu u_X)_X \\ \frac{(\gamma-1)M}{R}(\kappa T_X)_X \end{pmatrix} \quad (10)$$

for $0 < X$. Linearize the system (8) around a constant state $\hat{u}, \hat{\sigma}, \hat{T}$, $\hat{x} = X + \hat{u}t$, to obtain

$$\begin{pmatrix} u \\ \sigma \\ T \\ x_X \end{pmatrix}_t = \begin{pmatrix} 0 & 1/m_0 & -\alpha \hat{p}_\epsilon / m_0 & \hat{p}_\rho \\ (2\mu_e + \lambda_e) & 0 & 0 & 0 \\ \frac{\hat{\sigma} - \hat{p}}{\alpha m_0} & 0 & 0 & 0 \\ 1 & 0 & 0 & 0 \end{pmatrix} \begin{pmatrix} u \\ \sigma \\ T \\ x_X \end{pmatrix}_X + \begin{pmatrix} 0 \\ 0 \\ \frac{\kappa_e}{\alpha m_0} T_{XX} \\ 0 \end{pmatrix} \quad (11)$$

for $X < 0$. The notations $\hat{p}_\epsilon, \hat{p}_\rho$ are the partial derivatives of the equation of state as a function $p = p(\epsilon, \rho)$ evaluated at the linearization state. The linearized mass conservation is

$$\hat{\rho} x_X = -\rho. \quad (12)$$

We introduce the vector of unknowns in the fluid and the solid respectively as $\mathbf{q}^{(f)} = (\rho \ u \ T)$ and $\mathbf{q}^{(s)} = (u \ \sigma \ T \ x_X)$, and rewrite (10) and (11) in matrix form as

$$\mathbf{q}_t^{(s)} + A_s \mathbf{q}_X^{(s)} = B_s \mathbf{q}_{XX}^{(s)} \quad X < 0 \quad (13)$$

$$\mathbf{q}_t^{(f)} + A_f \mathbf{q}_X^{(f)} = B_f \mathbf{q}_{XX}^{(f)} \quad X > 0, \quad (14)$$

where the definition of the matrices A_s, B_s, A_f , and B_f are immediate from (10) and (11). B_s and B_f are diagonal matrices. The eigenvalues of A_f are $u - c, u, u + c$ where $c = \sqrt{\gamma p / \rho}$, which shows that the fluid equations are hyperbolic in the inviscid limit for positive pressure and density. A_s has eigenvalues $0, 0, -a$, and a , where

$$a^2 = \frac{2\mu_e + \lambda_e}{m_0} + \frac{\hat{p} - \hat{\sigma}}{m_0^2} \hat{p}_\epsilon + \hat{p}_\rho.$$

Linearization around the reference state with $\hat{p}^{(s)} - \hat{\sigma} = \hat{p}^{(f)}$, because of (5), guarantees, since $\hat{p}^{(f)} > 0$, that $\hat{p}^{(s)} - \hat{\sigma} > 0$. Hence, $a^2 > 0$ and A_s has real eigenvalues under the additional assumptions $\hat{p}_\epsilon > 0$ and $\hat{p}_\rho > 0$, for example, the ideal gas law $p = (\gamma - 1)\rho\epsilon$.

The linearization states must satisfy the interface conditions, that \hat{u} in the fluid and in the solid are equal, and that this also holds for \hat{T} . Furthermore, mass conservation shows that $\hat{\rho}^{(s)} = m_0$.

At $X = 0$ the interface conditions (4), (6), and (7) are unchanged for the linearized problem. Linearization of (5) around the reference state with $\hat{p}^{(f)} = \hat{p}^{(s)} - \hat{\sigma}$ gives

$$-\frac{\hat{R}T}{M}\rho - \frac{\hat{\rho}R}{M}T + \frac{4\mu}{3}u_x = \sigma - \hat{p}_\epsilon\alpha T - \hat{p}_\rho\rho. \quad (15)$$

In order to prove an energy estimate, we first transform the systems (13) and (14) to symmetric form. This is done by the diagonal matrix

$$Y_s = \text{diag} \left(1/\sqrt{m_0}, \sqrt{2\mu + \lambda}, \sqrt{\hat{p}^{(f)}}/(\alpha\sqrt{m_0\hat{p}_\epsilon}), 1/\sqrt{m_0\hat{p}_\rho} \right) \quad (16)$$

for (13) and by

$$Y_f = \text{diag} \left(\sqrt{\hat{\rho}M/(R\hat{T})}, 1/\sqrt{\hat{\rho}}, \sqrt{(\gamma - 1)\hat{T}M/(\hat{\rho}R)} \right) \quad (17)$$

for (14). Denote $\mathbf{w}^{(s)} = Y_s^{-1}\mathbf{q}^{(s)}$ and $\mathbf{w}^{(f)} = Y_f^{-1}\mathbf{q}^{(f)}$. The symmetrized equations,

$$\mathbf{w}_t^{(s)} + S_s\mathbf{w}_X^{(s)} = B_s\mathbf{w}_{XX}^{(s)} \quad X < 0 \quad (18)$$

$$\mathbf{w}_t^{(f)} + S_f\mathbf{w}_X^{(f)} = B_f\mathbf{w}_{XX}^{(f)} \quad X > 0, \quad (19)$$

are obtained by left multiplication of (13) and (14) by Y_s^{-1} and Y_f^{-1} respectively. The symmetric matrices are

$$S_s = \begin{pmatrix} 0 & -\sqrt{\frac{2\mu_e + \lambda_e}{m_0}} & \frac{\sqrt{\hat{p}_\epsilon\hat{p}}}{m_0} & -\sqrt{\hat{p}_\rho} \\ \cdot & 0 & 0 & 0 \\ \cdot & \cdot & 0 & 0 \\ \cdot & \cdot & \cdot & 0 \end{pmatrix} \quad S_f = \begin{pmatrix} 0 & \sqrt{\frac{R\hat{T}}{M}} & 0 \\ \cdot & 0 & \sqrt{\frac{R(\gamma-1)\hat{T}}{M}} \\ \cdot & \cdot & 0 \end{pmatrix}.$$

for the solid and fluid respectively. B_s and B_f are unchanged by the symmetrizing transformation, because they are diagonal.

Define the scalar product for any two functions on $X < 0$ by

$$(p, q)_- = \int_{-\infty}^0 p(X, t)q(X, t) dX,$$

and similarly on $X > 0$,

$$(p, q)_+ = \int_0^{\infty} p(X, t)q(X, t) dX.$$

The corresponding norms are denoted by $\|q\|_-^2 = (q, q)_-$ and $\|q\|_+^2 = (q, q)_+$. The following theorem states well-posedness of the linearized fluid/structure problem.

Theorem 1 *Consider the equations (19) for $X > 0$ and (18) for $X < 0$, coupled by (4), (15), (6), and (7) at $X = 0$. Assume that the solutions vanish when $X \rightarrow \pm\infty$. Furthermore, assume that $p^{(s)}(\epsilon, \rho)$ has positive partial derivatives, $p_\epsilon^{(s)} > 0$ and $p_\rho^{(s)} > 0$. Then the estimate*

$$\|\mathbf{w}^{(s)}(t)\|_-^2 + \|\mathbf{w}^{(f)}(t)\|_+^2 \leq \|\mathbf{w}^{(s)}(0)\|_-^2 + \|\mathbf{w}^{(f)}(0)\|_+^2 \quad (20)$$

holds for all $t > 0$.

Proof: The standard estimate

$$\begin{aligned} \frac{1}{2} \frac{d}{dt} \|\mathbf{w}\|^2 &= (\mathbf{w}, \mathbf{w}_t) = -(\mathbf{w}, S\mathbf{w}_x) + (\mathbf{w}, B\mathbf{w}_{xx}) \\ &= -\frac{1}{2} \mathbf{w}^T S \mathbf{w}|_b - (\mathbf{w}_x, B\mathbf{w}_x) + \mathbf{w}^T B \mathbf{w}_x|_b, \end{aligned} \quad (21)$$

for the PDE $\mathbf{w}_t + S\mathbf{w}_x = B\mathbf{w}_{xx}$ with symmetric S holds, because partial integration and the symmetry of S gives

$$(\mathbf{w}, S\mathbf{w}_x) = -(\mathbf{w}_x, S\mathbf{w}) + \mathbf{w}^T S \mathbf{w}|_b = -(S\mathbf{w}_x, \mathbf{w}) + \mathbf{w}^T S \mathbf{w}|_b$$

and $(\mathbf{w}, S\mathbf{w}_x) = (1/2)\mathbf{w}^T S \mathbf{w}|_b$ follows. The notation $|_b$ denotes restriction to the boundary. It follows that

$$\begin{aligned} \frac{1}{2} \frac{d}{dt} (\|\mathbf{w}^{(s)}(t)\|_-^2 + \|\mathbf{w}^{(f)}(t)\|_+^2) &= \\ \frac{1}{2} & \left(-(\mathbf{w}^{(s)})^T S_s \mathbf{w}^{(s)}|_0 + (\mathbf{w}^{(f)})^T S_f \mathbf{w}^{(f)}|_0 \right) + (\mathbf{w}^{(s)})^T B_s \mathbf{w}_x^{(s)}|_0 \\ & - (\mathbf{w}^{(f)})^T B_f \mathbf{w}_x^{(f)}|_0 - (\mathbf{w}_x^{(s)}, B_s \mathbf{w}_x^{(s)})_- - (\mathbf{w}_x^{(f)}, B_f \mathbf{w}_x^{(f)})_+, \end{aligned} \quad (22)$$

where $|_0$ is restriction to $X = 0$. The interface condition is obtained by requiring

$$\frac{1}{2} \left(-(\mathbf{w}^{(s)})^T S_s \mathbf{w}^{(s)}|_0 + (\mathbf{w}^{(f)})^T S_f \mathbf{w}^{(f)}|_0 \right) + (\mathbf{w}^{(s)})^T B_s \mathbf{w}_x^{(s)}|_0 - (\mathbf{w}^{(f)})^T B_f \mathbf{w}_x^{(f)}|_0 = 0,$$

which written out in terms of the original variables is equivalent with

$$\begin{aligned} \frac{1}{2} u^{(s)} (\sigma - \hat{p}_\rho \rho^{(s)} - \alpha \hat{p}_\epsilon T^{(s)}) + \frac{1}{2} u^{(f)} \left(\frac{R}{M} \hat{T} \rho^{(f)} + \frac{R}{M} \hat{\rho} T^{(f)} - \frac{4}{3} \mu u_X^{(f)} \right) + \\ \frac{1}{\hat{T}} \kappa_e T^{(s)} T_X^{(s)} - \frac{1}{\hat{T}} \kappa T^{(f)} T_X^{(f)} = 0, \quad (23) \end{aligned}$$

where all variables are evaluated at $X = 0$. It is straightforward to verify that interface conditions (4), (15), (6), and (7) indeed make the left hand side of (23) equal to zero. The remaining terms of (22) give,

$$\frac{1}{2} \frac{d}{dt} \left(\|\mathbf{w}^{(s)}(t)\|_-^2 + \|\mathbf{w}^{(f)}(t)\|_+^2 \right) = -(\mathbf{w}_x^{(s)}, B_s \mathbf{w}_x^{(s)})_- - (\mathbf{w}_x^{(f)}, B_f \mathbf{w}_x^{(f)})_+ \leq 0,$$

because B_f and B_s are positive definite. The energy estimate (20) follows. \square

4 Discretization in one space dimension

Introduce a uniform grid with grid spacing h on the domain in Fig. 2, in the Lagrangian coordinate, $X_j = jh$. Let the fluid/structure interface be located at the grid point $j = 0$. The dependent variables of the fluid equations at the grid point X_j , $(\rho_j, \rho_j u_j, e_j)$, are defined for $j \geq 0$ and the dependent variables of the elasticity equations, $(u_j, \sigma_j, \epsilon_j, x_j)$ are defined for $j \leq 0$. Hence, both solid and fluid variables are defined at the interface grid point $X_0 = 0$.

4.1 Discretization by summation-by-parts finite differences

Summation-by-parts (SBP) finite difference operators satisfy a discrete integration by parts identity. For a discrete weighted scalar product defined on $j \leq 0$,

$$(u, v)_{h-} = h \sum_{j=-\infty}^0 a_j^{(-)} u_j v_j$$

a summation-by-parts finite difference operator, is a difference operator, D_L that satisfies

$$(u, D_L v)_{h-} = -(D_L u, v)_{h-} + u_0 v_0 \quad (24)$$

for grid functions u_j and v_j defined on $j \leq 0$. Here D_L is a standard centered difference operator away from the boundary. Near the boundary $j = 0$, D_L is biased toward the left and only uses function values with $j \leq 0$. The weights in the norm $a_j^{(-)} > 0$ are equal to one away from the boundary, and are modified to satisfy (24) near the boundary. For details on how to derive operators and scalar products, see [11, 13], where also example operators of orders up to 4 at the boundaries and up to 8 away from the boundaries are given. The scalar product for $j \geq 0$ is defined similarly as

$$(u, v)_{h+} = h \sum_{j=0}^{\infty} a_j^{(+)} u_j v_j,$$

and a finite difference operator on $j \geq 0$, biased to the right at $j = 0$, D_R , can be made to satisfy

$$(u, D_R v)_{h+} = -(D_R u, v)_{h+} - u_0 v_0$$

for grid functions, u_j and v_j defined on $j \geq 0$. The corresponding discrete norms are denoted by $\|u\|_{h-}^2 = (u, u)_{h-}$ and $\|u\|_{h+}^2 = (u, u)_{h+}$.

The semi-discrete approximation of (14) and (13) is obtained by replacing all spatial derivatives by SBP difference operators. In the SBP framework, boundary conditions can be imposed by projection [11], by a penalty term (so called SAT boundary condition) [3], or by use of a ghost point [10]. Here, we use projections to impose the interface conditions at $j = 0$. The projection method introduces a projection operator, P , that projects a general grid function onto the set of grid functions that satisfy the interface conditions. This operator is applied after each time step. In a semi-discrete approximation, this amounts to solving the equations

$$\frac{d}{dt} \mathbf{q}_j^{(s)} + P_s A_s D_L \mathbf{q}_j^{(s)} = P_s B_s D_L^2 \mathbf{q}_j^{(s)} \quad j \leq 0 \quad (25)$$

$$\frac{d}{dt} \mathbf{q}_j^{(f)} + P_f A_f D_R \mathbf{q}_j^{(f)} = P_f B_f D_R^2 \mathbf{q}_j^{(f)} \quad j \geq 0, \quad (26)$$

where P_s and P_f are the projections on the solid and fluid variables respectively. The discrete form of the interface conditions is

$$u_0^{(s)} = u_0^{(f)} \quad (27)$$

$$\sigma_0 - \hat{p}_\epsilon \alpha T_0^{(s)} - \hat{p}_\rho \rho_0^{(s)} = -\frac{\hat{R}T}{M} \rho_0^{(f)} - \frac{\hat{\rho}R}{M} T_0^{(f)} + \frac{4\mu}{3} D_R u_0^{(f)} \quad (28)$$

$$T_0^{(s)} = T_0^{(f)} \quad (29)$$

$$\kappa_e D_L T_0^{(s)} = \kappa D_R T_0^{(f)}. \quad (30)$$

The following theorem states that if the projections are applied in the symmetric variables, an energy estimate follows.

Theorem 2 Define $P_s = Y_s Q_s Y_s^{-1}$ and $P_f = Y_f Q_f Y_f^{-1}$, where Q_s and Q_f are projections to the interface condition acting on the symmetric variables, i.e., grid functions $(Q_s \mathbf{w}^{(s)}, Q_f \mathbf{w}^{(f)})$ that satisfy the discrete interface conditions (27)–(30), and minimize $\|\mathbf{w}^{(s)} - Q_s \mathbf{w}^{(s)}\|_{h-}^2 + \|\mathbf{w}^{(f)} - Q_f \mathbf{w}^{(f)}\|_{h+}^2$. Then the energy estimate for the symmetric variables in the discrete norm,

$$\frac{d}{dt} (\|\mathbf{w}^{(s)}(t)\|_{h-}^2 + \|\mathbf{w}^{(f)}(t)\|_{h+}^2) \leq 0$$

holds.

Proof: The first step is to transform (25) and (26) to symmetric form by left multiplication of (16) and (17). Symmetrization of the elasticity equations ($j \leq 0$) gives

$$\frac{d}{dt} \mathbf{w}_j^{(s)} + Y_s^{-1} P_s Y_s S_s D_L \mathbf{w}_j^{(s)} = Y_s^{-1} P_s Y_s B_s D_L^2 \mathbf{w}_j^{(s)},$$

and hence

$$\frac{d}{dt} \mathbf{w}_j^{(s)} + Q_s S_s D_L \mathbf{w}_j^{(s)} = Q_s B_s D_L^2 \mathbf{w}_j^{(s)}. \quad (31)$$

Multiplication of (31) and the projection property $Q_s^2 = Q_s$ shows that

$$\frac{d}{dt} (\mathbf{w}_j^{(s)} - Q_s \mathbf{w}_j^{(s)}) = 0 \Rightarrow \mathbf{w}_j(t) = Q_s \mathbf{w}_j(t). \quad (32)$$

if the initial data satisfies the interface conditions. The estimate for $j \leq 0$ becomes,

$$\begin{aligned} \frac{1}{2} \frac{d}{dt} \|\mathbf{w}^{(s)}(t)\|_{h-}^2 &= (\mathbf{w}^{(s)}, \mathbf{w}_t^{(s)})_{h-} = -(Q_s S_s D_L \mathbf{w}^{(s)}, \mathbf{w}^{(s)})_{h-} \\ &+ (Q_s B_s D_L^2 \mathbf{w}^{(s)}, \mathbf{w}^{(s)})_{h-} = -(S_s D_L \mathbf{w}^{(s)}, \mathbf{w}^{(s)})_{h-} + (B_s D_L^2 \mathbf{w}^{(s)}, \mathbf{w}^{(s)})_{h-} \\ &- ((Q_s - I) S_s D_L \mathbf{w}^{(s)}, \mathbf{w}^{(s)})_{h-} + ((Q_s - I) B_s D_L^2 \mathbf{w}^{(s)}, \mathbf{w}^{(s)})_{h-} \quad (33) \end{aligned}$$

where the last two terms are zero because of (32), and the orthogonality of the projection. The SBP property (24) gives

$$\begin{aligned} \frac{1}{2} \frac{d}{dt} \|\mathbf{w}^{(s)}(t)\|_{h-}^2 &= -(S_s D_L \mathbf{w}^{(s)}, \mathbf{w}^{(s)})_{h-} + (B_s D_L^2 \mathbf{w}^{(s)}, \mathbf{w}^{(s)})_{h-} \\ &= -\frac{1}{2} (\mathbf{w}_0^{(s)})^T S_s \mathbf{w}_0^{(s)} + (\mathbf{w}^{(s)})_0^T B_s D_L \mathbf{w}_0^{(s)} - (D_L \mathbf{w}^{(s)}, B_s D_L \mathbf{w}^{(s)})_{h-} \quad (34) \end{aligned}$$

in the same way as partial integration gives the estimate for the continuous problem. The estimate for the fluid equations on $j \geq 0$ is analogous and is not given here. The resulting discrete interface condition,

$$-\frac{1}{2} (\mathbf{w}_0^{(s)})^T S_s \mathbf{w}_0^{(s)} + \frac{1}{2} (\mathbf{w}_0^{(f)})^T S_f \mathbf{w}_0^{(f)} + (\mathbf{w}_0^{(s)})^T B_s D_L \mathbf{w}_0^{(s)} - (\mathbf{w}_0^{(f)})^T B_f D_R \mathbf{w}_0^{(f)} = 0, \quad (35)$$

eliminates all interface contributions to the time derivative of the norm. Written out in original variables (35) becomes identical to (23) evaluated at $j = 0$ and with derivatives in X replaced by D_L or D_R for solid or fluid variables respectively. It is straightforward to verify that (27)–(30) satisfy (35). Therefore, the interface terms do not give any contribution to the time derivative of the norm, and the estimate follows. \square

In each time step (or Runge-Kutta stage) in the fully discretized computation, the solution is first updated at all grid points, including the interface point $j = 0$, and then this updated solution is projected to the interface conditions. The projection for the temperatures means solving the two equations (29), (30) directly for the two temperatures $T_0^{(s)}$ and $T_0^{(f)}$. There is always a unique solution, because the coefficients of the $j = 0$ element in the completely backward operator D_L and the completely forward operator D_R have opposite signs. Let us denote the variables after the application of the SBP discretization but before imposing the interface condition by $\tilde{\mathbf{w}}$. Denote the

difference operator approximating $du/dx(x_0)$ by

$$D_R u_0 = \frac{1}{h} \sum_{k=0}^m \beta_k u_k$$

where $m+1$ is the stencil width. Assume that the interface temperature has been determined by (29), (30). The interface conditions for the remaining variables, imposed by projections are given in the following theorem.

Theorem 3 *Assume that $p^{(s)} = 0$, i.e., that the solid is purely elastic. The interface conditions imposed as a projection are*

$$u_0^{(s)} = \tilde{u}_0^{(s)} - a/m_0 \quad \sigma_0 = \tilde{\sigma}_0 - (2\mu_e + \lambda_e)b \quad (36)$$

for the variables in the solid. Similarly, the projection gives the update

$$u_0^{(f)} = \tilde{u}_0^{(f)} + a/\hat{\rho} + b \frac{4\mu}{3\hat{\rho}} \frac{\beta_0}{h} \quad u_j^{(f)} = \tilde{u}_j^{(f)} + b \frac{4\mu}{3\hat{\rho}} \frac{a_0^{(+)} \beta_0}{a_j^{(+)} h}, \quad j = 1, \dots, m \quad (37)$$

for the fluid velocity, and

$$\rho_0^{(f)} = \tilde{\rho}_0^{(f)} - \hat{\rho}b \quad (38)$$

for the fluid density. a and b are two Lagrangian multipliers obtained as the solution of the linear system of equations

$$\begin{aligned} \left(\frac{1}{m_0} + \frac{1}{\hat{\rho}}\right)a + \frac{4\mu}{3\hat{\rho}} \frac{\beta_0}{h} b &= \tilde{u}_0^{(s)} - \tilde{u}_0^{(f)} \\ \frac{4\mu}{3\hat{\rho}} \frac{\beta_0}{h} a + (2\mu_e + \lambda_e + \frac{R\hat{T}\hat{\rho}}{M} + \frac{16\mu^2}{9\hat{\rho}h^2} \sum_{k=0}^m \frac{a_0^{(+)}}{a_k^{(+)}} \beta_k^2) b &= \tilde{\sigma}_0 + \frac{R\hat{T}}{M} \tilde{\rho}_0^{(f)} \\ &\quad + \frac{R\hat{\rho}}{M} T_0 - \frac{4\mu}{3} D_R \tilde{u}_0^{(f)}. \end{aligned} \quad (39)$$

Proof: The projections are defined as functions $\mathbf{w}^{(s)}$ and $\mathbf{w}^{(f)}$ that minimize

$$||\tilde{\mathbf{w}}^{(s)} - \mathbf{w}^{(s)}||_{h-}^2 + ||\tilde{\mathbf{w}}^{(f)} - \mathbf{w}^{(f)}||_{h+}^2$$

and satisfy the interface conditions. Introducing the two Lagrangian multipliers l_1 and l_2 and writing out the norm expressions, using symmetric

variables, leads to the Lagrangian

$$\begin{aligned}
L = & \sum_{j=-\infty}^0 a_j^{(-)} (\sqrt{m_0} (\tilde{u}_j^{(s)} - u_j^{(s)}))^2 + \sum_{j=0}^{\infty} a_j^{(+)} (\sqrt{\hat{\rho}} (\tilde{u}_j^{(f)} - u_j^{(f)}))^2 \\
& + \sum_{j=-\infty}^0 a_j^{(-)} \left(\frac{1}{2\mu_e + \lambda_e} (\tilde{\sigma}_j^{(s)} - \sigma_j^{(s)}) \right)^2 + \sum_{j=0}^{\infty} a_j^{(+)} \left(\sqrt{\frac{R\hat{T}}{M\hat{\rho}}} (\tilde{\rho}_j^{(f)} - \rho_j^{(f)}) \right)^2 \\
& + l_1 (u_0^{(s)} - u_0^{(f)}) + l_2 \left(\sigma_0 + \frac{R\hat{T}}{M} \rho_0^{(f)} + \frac{\hat{\rho}R}{M} T_0 - \frac{4\mu}{3} D_R u_0^{(f)} \right). \quad (40)
\end{aligned}$$

It is straightforward to conclude from (40) that the only variables that need to be modified are $\tilde{u}_0^{(s)}$, $\tilde{\sigma}_0$, $\tilde{\rho}_0^{(f)}$, and $\tilde{u}_0^{(f)}, \dots, \tilde{u}_m^{(f)}$. The zero gradient condition

$$\frac{\partial L}{\partial u_0^{(s)}} = -m_0 a_0^{(-)} (\tilde{u}_0^{(s)} - u_0^{(s)}) + l_1 = 0 \quad (41)$$

$$\frac{\partial L}{\partial u_0^{(f)}} = -\hat{\rho} a_0^{(+)} (\tilde{u}_0^{(f)} - u_0^{(f)}) - l_1 - l_2 \frac{4\mu\beta_0}{3h} = 0 \quad (42)$$

$$\frac{\partial L}{\partial u_j^{(f)}} = -\hat{\rho} a_j^{(+)} (\tilde{u}_j^{(f)} - u_j^{(f)}) - l_2 \frac{4\mu\beta_j}{3h} = 0 \quad j = 1, \dots, m \quad (43)$$

$$\frac{\partial L}{\partial \sigma_0} = \frac{a_0^{(-)}}{2\mu_e + \lambda_e} (\tilde{\sigma}_0 - \sigma_0) + l_2 = 0 \quad (44)$$

$$\frac{\partial L}{\partial \rho_0^{(f)}} = a_0^{(-)} \frac{R\hat{T}}{M\hat{\rho}} (\tilde{\rho}_0^{(f)} - \rho_0^{(f)}) + l_2 \frac{R\hat{T}}{M} = 0 \quad (45)$$

gives (36)–(38), after rescaling $a = l_1/a_0^{(+)}$ and $b = l_2/a_0^{(+)}$. Note that $a_0^{(-)} = a_0^{(+)}$, since the same summation by parts norm is used on the two domains. Finally, insertion of (36)–(38) into the interface conditions (27) and (28) gives (39). \square

Note that by combining the velocities from (36) and (37), the common interface velocity can be written

$$\frac{\hat{\rho}^{(f)} \tilde{u}_0^{(f)} + m_0 \tilde{u}_0^{(s)}}{\hat{\rho}^{(f)} + m_0} + b \frac{4\mu}{3} \frac{1}{m_0 + \hat{\rho}} \frac{\beta_0}{h}. \quad (46)$$

In the inviscid case, $\mu = 0$, (46) is the same mass weighted average for the boundary velocity that was independently derived from a characteristic

boundary condition and proved to be stable for explicit time discretizations in [7]. Similarly, by using the notation

$$\tilde{\sigma}_0^{(f)} = -\frac{R\hat{\rho}}{M}T_0 - \frac{R\hat{T}}{M}\tilde{\rho}_0^{(f)} + \frac{4\mu}{3}D_R\tilde{u}_0^{(f)}$$

and

$$\hat{p} = \frac{R\hat{T}\hat{\rho}}{M}, \quad (47)$$

the common interface stress can be written

$$\frac{\hat{p}\tilde{\sigma}_0^{(s)} + (2\mu_e + \lambda_e)\tilde{\sigma}_0^{(f)}}{\hat{p} + 2\mu_e + \lambda_e} + (2\mu_e + \lambda_e)\frac{4\mu}{3}\left(\frac{a\beta_0}{\hat{\rho}h} + b\frac{4\mu}{3\hat{\rho}h^2}\sum_{k=0}^m\frac{a_0^{(+)}}{a_k^{(+)}}\beta_k^2\right)$$

which again, in the inviscid case, is the same weighted average stress that was proved stable for explicit time discretizations in [7].

4.2 Non-linear coupled problem

The straightforward generalization of (25) and (26) to the complete non-linear equations (8) and (9) is

$$\frac{d}{dt}\begin{pmatrix} u \\ \sigma \\ T \\ x \end{pmatrix}_j = \begin{pmatrix} \frac{1}{m_0}D_L(\sigma_j - p_j) \\ \frac{2\mu_e + \lambda_e}{D_L x_j}D_L u_j \\ \frac{\sigma_j - p_j}{m_0}D_L u_j + D_L\left(\frac{\kappa_e}{D_L x_j}D_L T_j\right) \\ u_j \end{pmatrix} \quad (48)$$

on $j \leq 0$, and

$$\frac{d}{dt}\begin{pmatrix} \rho \\ \rho u \\ e \end{pmatrix}_j + \begin{pmatrix} D_R(\rho_j u_j - u_0^{(f)}\rho_j) \\ D_R(\rho_j u_j^2 + p_j - u_0^{(f)}\rho_j u_j) - \frac{4}{3}\mu D_R^2 u_j \\ D_R(u_j(e_j + p_j) - u_0^{(f)}e_j) - \frac{4}{3}\mu D_R(u_j D_R u_j) - D_R(\kappa D_R T_j) \end{pmatrix} = 0. \quad (49)$$

on $j \geq 0$. The grid derivative x_X was linearized to one in the analysis in Sec. 4.1, but it should be present in the full equations. Therefore, the

temperature interface conditions also takes into account that the gradient is defined in the Eulerian frame, and become

$$T_0^{(s)} = T_0^{(f)} \quad \kappa_e \frac{1}{D_L x_0} D_L T_0^{(s)} = \kappa D_R T_0^{(f)}, \quad (50)$$

which determine the two unknowns $T_0^{(s)}$ and $T_0^{(f)}$. The projection conditions (36)–(37) are kept without changes. There are several possibilities for the linearization density $\hat{\rho}$. In Section 5 we have used the value one point into the fluid, i.e., $\hat{\rho} = \rho_1^{(f)}$. Similarly, the linearization pressure needed below is set to $\hat{p} = p_1^{(f)}$ in the numerical experiments. (38) is replaced by the similar update for the pressure,

$$p_0^{(f)} = \tilde{p}_0^{(f)} - \hat{p}b, \quad (51)$$

where

$$\tilde{p}_0^{(f)} = \frac{R\hat{\rho}_0^{(f)}T_0}{M}.$$

The second equation of (39) is written in terms of the pressure as

$$\frac{4\mu}{3\hat{\rho}} \frac{\beta_0}{h} a + (2\mu_e + \lambda_e + \hat{p} + \frac{16\mu^2}{9\hat{\rho}h^2} \sum_{k=0}^m \frac{a_0^{(+)}}{a_k^{(+)}} \beta_k^2) b = \tilde{\sigma}_0 + \tilde{p}_0^{(f)} - \frac{4\mu}{3} D_R \tilde{u}_0^{(f)}. \quad (52)$$

To summarize, the interface conditions for the non-linear coupled problem is (50), (36), (37), and (51), where the parameters a and b are determined by the first equation of (39) and (52). Finally, after the fluid interface pressure and temperature are determined, the interface fluid density $\rho_0^{(f)}$, is adjusted to satisfy the perfect gas law.

Note that (51) is equivalent with the stress continuity condition

$$\sigma_0 = -p_0^{(f)} + \frac{4\mu}{3} D_R u_0^{(f)} \quad (53)$$

for any choice of the linearization states $\hat{\rho}$ and \hat{p} . This is seen by using (37) and the stress update $\sigma_0 = \tilde{\sigma}_0 - (2\mu_e + \lambda_e)b$ to eliminate $\tilde{u}_j^{(f)}$ and $\tilde{\sigma}_0$ from (52). In practical computations, we use (53) instead of (51) to determine $p_0^{(f)}$.

The interface is always located at $j = 0$, but because the grid moves in both domains, a fixed boundary for the fluid in the Eulerian domain becomes a moving boundary in the frame of the grid, and has to be treated specially.

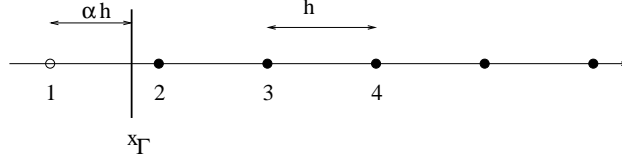


Figure 3: Grid points with boundary between points 1 and 2.

4.3 Wall boundary

In some of the numerical examples below, the grids are moving while the boundary of the computational domain is fixed. In this case the boundary condition at the fixed domain boundary is treated as a moving embedded boundary in the frame of the moving grid. The situation is outlined in Fig. 3. The points x_2, x_3, \dots , are interior to the computational domain, x_1 is the ghost point. The boundary is located at $x_\Gamma(t)$ and it is fixed, but when viewed in the moving grid frame, the location of the boundary obeys the equation

$$\frac{dx_\Gamma}{dt} = -s \quad (54)$$

where s is the velocity of the grid. Solving (54) together with the other equations determines the boundary location at each time level. In Fig. 3, the ghost point x_1 is the first point outside the domain. The distance between the ghost point and the boundary is denoted αh , where h is the grid spacing. The Dirichlet boundary condition

$$u(x_\Gamma) = g,$$

with given data g , is imposed by the second order extrapolation formula

$$\frac{(1-\alpha)(2-\alpha)}{2}u_1 + \alpha(2-\alpha)u_2 + \frac{\alpha(1-\alpha)}{2}u_3 + \eta(u_1 - 2u_2 + u_3) = g. \quad (55)$$

η is an artificial parameter that is used to prevent division by zero, see [8]. The value of the solution at the ghost point, x_1 , is found by solving (55) for u_1 . A similar formula for Neumann boundary conditions is easily derived, see [9]. Equation (55) is straightforward to formally generalize to fourth order by increasing the extrapolation order, and the order of difference in the artificial term. This fourth order generalization worked well in the numerical experiments below, a proof of stability is outside the scope of this article.

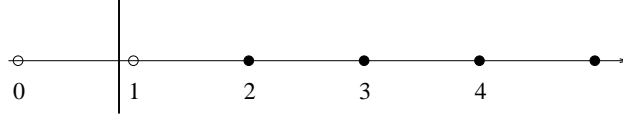


Figure 4: Boundary has moved backwards, 1 becomes interior point and 0 becomes the new ghost point.

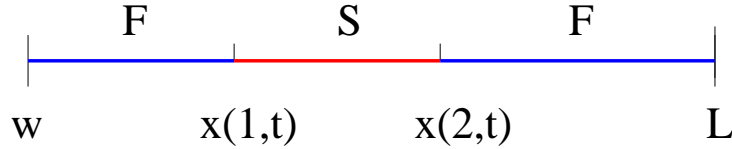


Figure 5: Computational domain for the numerical experiments.

If the boundary moves to the left in Fig. 3, it is possible that a ghost point becomes an interior point, and a new ghost point will have to be added. In Fig. 4, x_1 is the ghost point at time t_n that becomes an interior point at t_{n+1} , and x_0 becomes the new ghost point. To handle this, (55) is used to give values to both u_1 and u_0 at t_{n+1} (shifted one point left for u_0). α will then be negative for x_1 , but the coefficient in front of the ghost point, will be bounded away from zero, making it a well-defined boundary condition.

5 Numerical examples

The equations solved in this section are (48) and (49), coupled by the interface conditions described in Section 4.2. The time integration is explicit by the fourth-order accurate Runge-Kutta method. The time step is uniform in the domain, and determined as the smallest of the time steps required by the CFL constraints from the convection in the fluid, the diffusion in the fluid, the elastic wave speed in the solid, and the heat diffusion in the solid. The CFL number is 0.8. The computational domain is $w < x < L$, in the Eulerian coordinate. The domain of the fluid equations is $X < 1$ and $2 < X$, the domain for the solid equations is $1 < X < 2$. The grid mapping for the fluid is $x = X - 1 + x(1, t)$ and $x = X - 2 + x(2, t)$ for the left and right part of the fluid respectively. The lower and upper boundaries $x = w$ and

$x = L$ are embedded boundaries, as described in Section 4.3. The grid sizes in the computations below are always such that the two fluid/solid interfaces at $X = 1$ and $X = 2$ coincide with grid points. Figure 5 outlines the computational domain.

5.1 Test with the method of manufactured solutions

The implementation and formal accuracy is first verified by the method of manufactured solutions. Forcing functions on the right hand side of the equations are determined to give the exact solutions

$$\rho = 1 + \frac{1}{2} \sin(\omega X) \cos(t) \quad (56)$$

$$u = \sin(t) \cos(\omega X + \phi) \quad (57)$$

$$T = 10 + \sin(3t) \cos(2X) \quad (58)$$

in the fluid, and

$$u = dx(X, t)/dt \quad (59)$$

$$\sigma = \sin(t^2) \sin(\omega X) \quad (60)$$

$$T = 5 + \cos(t) \sin(3X) \quad (61)$$

$$x(X, t) = X + \frac{t^2}{2} (1 + X + \epsilon \sin(2\pi X)) \quad (62)$$

in the solid. The computational domain is $1/4 < x < 4$ with the solid in $1 < X < 2$. The exact solution is enforced by Dirichlet boundary conditions at the embedded boundaries at $x = 1/4$ and $x = 4$. The interface conditions are enforced at $X = 1$ and $X = 2$. The parameter values $\epsilon = 0.2$, $\omega = 2$, $\phi = 0.47$ are used. The material parameters are set to, $2\mu_e + \lambda_e = 10$, $\mu = 0.01$, $\kappa = 0.03$, $\kappa_e = 0.02$, $\alpha = 1$, $R/M = 1$, $\rho_0 = 2$, $\gamma = 1.4$. At the fluid/solid interfaces, the manufactured solutions are not continuous. The jump is prescribed as a forcing in the interface conditions, e.g., $u_0^{(f)} - u_0^{(s)} = g_u(t)$, where g_u is the jump in the velocity at the interface. These forcings are straightforward to introduce into the interface conditions. Figure 6 show the errors in L^2 -norm in the fluid and solid parts of the domain at time 0.45 for a sequence of computations with increasing grid refinements. The coarsest grid has $h = 0.05$, which corresponds to 75 grid points in the domain. The formal orders of the summation by parts difference operators are given as two

Fluid				Solid			
8/4	6/3	4/2	2/1	8/4	6/3	4/2	2/1
4.9	4.7	2.4	1.6	4.3	4.1	2.6	1.8

Table 1: Observed convergence exponents in L^2 -norm between the two finest grids.

numbers, x/y , for interior accuracy x and boundary accuracy y . The higher order methods 6/3 and 8/4 are clearly seen to give more accurate results than 2/1 and 4/2. The formal order in the boundary conditions at the embedded boundaries $x = w$ and $x = L$ are two for the 2/1 and 4/2 methods, and four for the 6/3 and 8/4. The explanation for the small difference in results with 6/3 and 8/4 could be that the errors from the embedded boundaries dominate over other errors on fine grids.

In hyperbolic problems with exact Dirichlet inflow data, there is a gain of one order in the numerical boundary conditions, so that the 8/4 method should converge with 5th order, the 6/3 with 4th order, etc. However at the fluid/solid interface the situation is not necessarily the same, because the imposed data at inflow is the value of the outflow variable of the neighboring domain. Therefore any error in the outflow variable from one domain, is transmitted to the inflow boundary on the other domain. Furthermore, in the computations here there are also diffusion terms present in the equations. Assuming local errors of order p at the boundary and/or interfaces for the $2p/p$ method, the L^2 norm error would have convergence exponent of $p + 1/2$. The observed convergence rates presented in Table 1 are in reasonable agreement with this, only the 6/3 method converges somewhat faster than expected. There is reasonable confidence that the implementation is correct.

5.2 Elastic rod in compressible fluid

The test example is an elastic rod in a compressible fluid. There is a gravitational force acting in the negative x -direction. The domain is the same as outlined in Fig. 5, with a solid wall boundary at $w = 0$, where adiabatic boundary conditions are imposed. The upper boundary of the fluid, $L = 6$, is treated as an open boundary with the artificial boundary conditions described in [5]. Initially the rod at rest is released and falls by its own weight

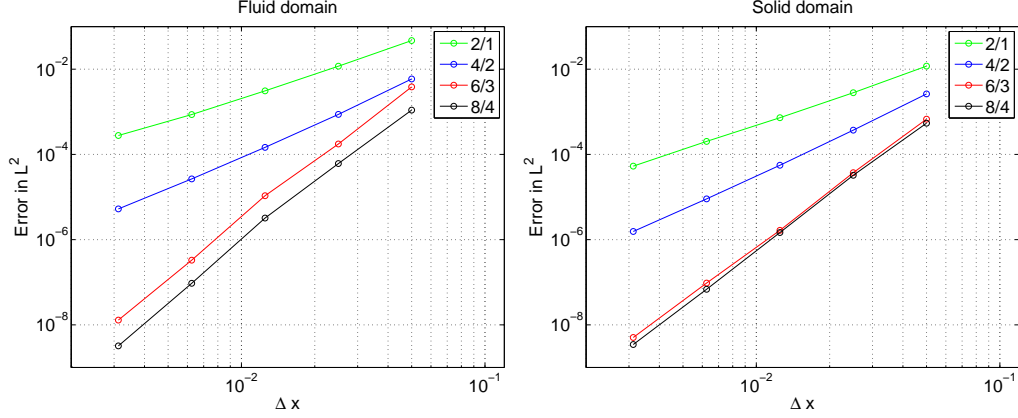


Figure 6: Errors in solution at time 0.45 in L^2 -norm for the fluid domain (left) and solid domain (right). Summation by parts finite difference approximation of formal orders interior/boundary, 2/1 (green), 4/2 (blue), 6/3 (red), and 8/4 (black).

towards the lower boundary $x = 0$. The fluid to the left of the rod is heated and compressed as it moves left. Eventually the rod bounces back right and a new cycle of left/right movement begins. Figures 7a–7d display the temperature during the left/right cycle. Red color indicates the elasticity equations and blue color the Navier-Stokes equations. The material parameters for the elastic material were

$$g = -10, \quad \kappa_e = 0.5, \quad 2\mu_e + \lambda_e = 10^5 \quad \rho_0 = 2700$$

and the pressure was identically zero, i.e., the material is purely elastic. The material parameters for the fluid were

$$\mu = 0.5, \quad \kappa = 0.7, \quad \gamma = 1.4, \quad R/M = 8.3145/0.029$$

These values were selected to get visible effects of many aspects of the equations, over a reasonable time. They do not necessarily represent physically reasonable materials. Figure 7a shows how the gas to the left is heated and compressed during the left movement. The leftmost point is reached in Fig. 7b. During the right movement in Fig. 7c, the gas is cooled by expansion. Back at the original position, shown in Fig. 7d, a minor temperature peak remains, because the solid is not cooled as quickly as the fluid. Figure

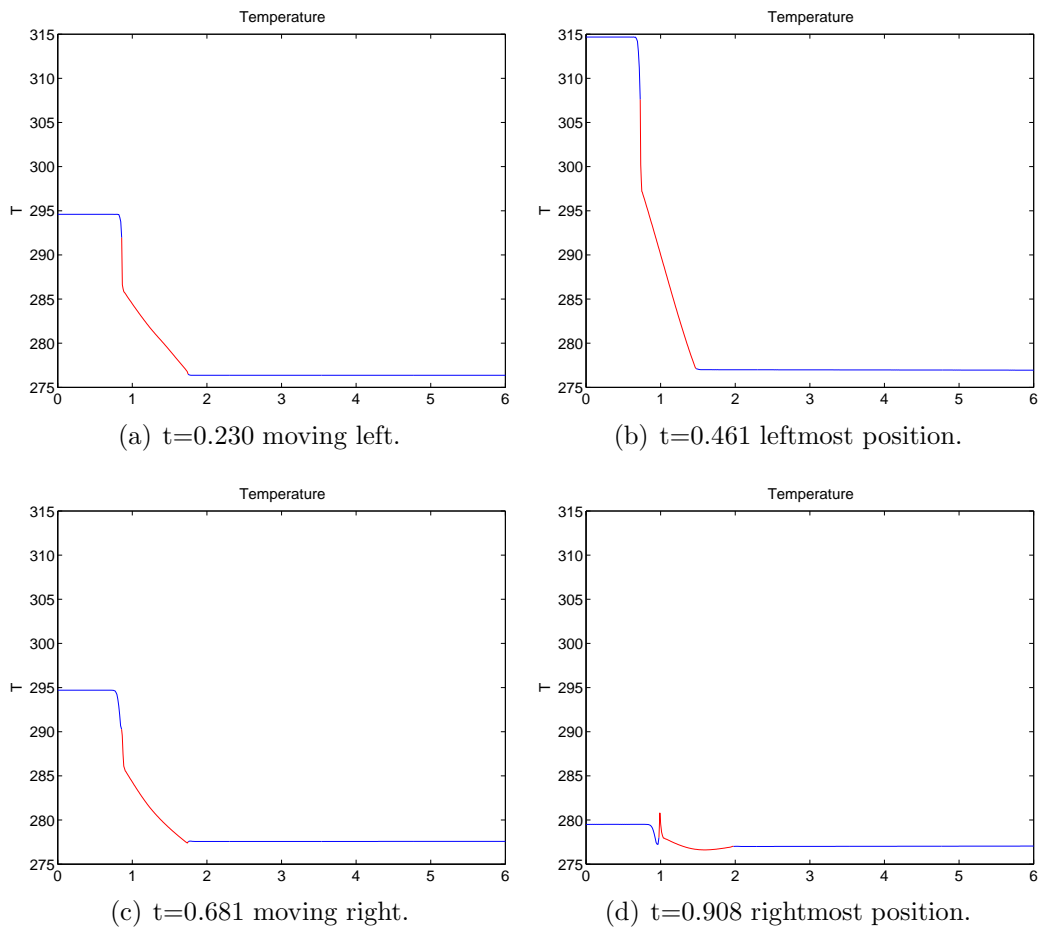
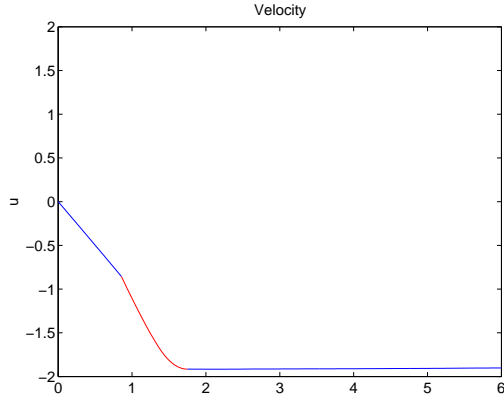
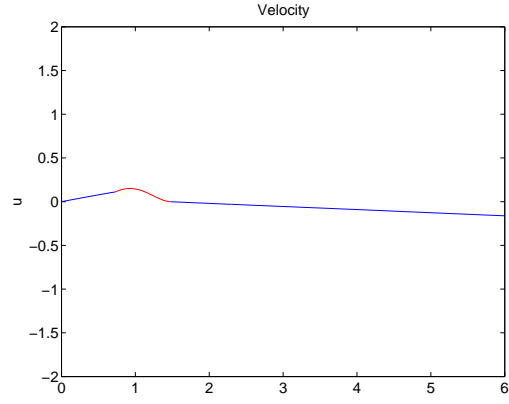


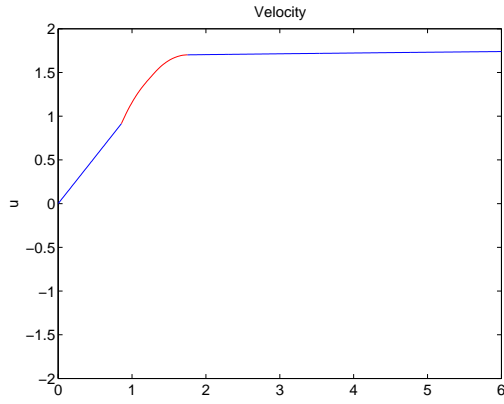
Figure 7: Temperature of the falling rod problem at four different times. Blue is fluid, red is solid. $4/2$ method. $h = 0.0125$.



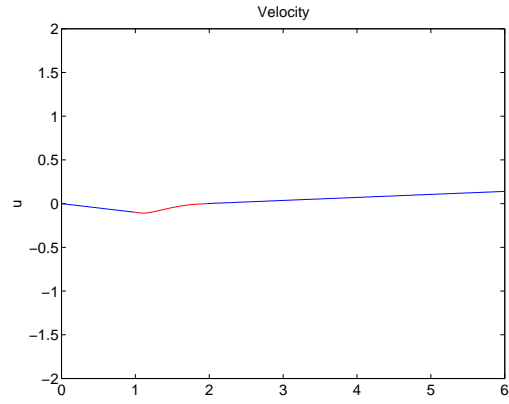
(a) $t=0.230$ moving left.



(b) $t=0.461$ leftmost position.



(c) $t=0.681$ moving right.



(d) $t=0.908$ rightmost position.

Figure 8: Velocity of the falling rod problem at four different times. Blue is fluid, red is solid. $4/2$ method. $h = 0.0125$.

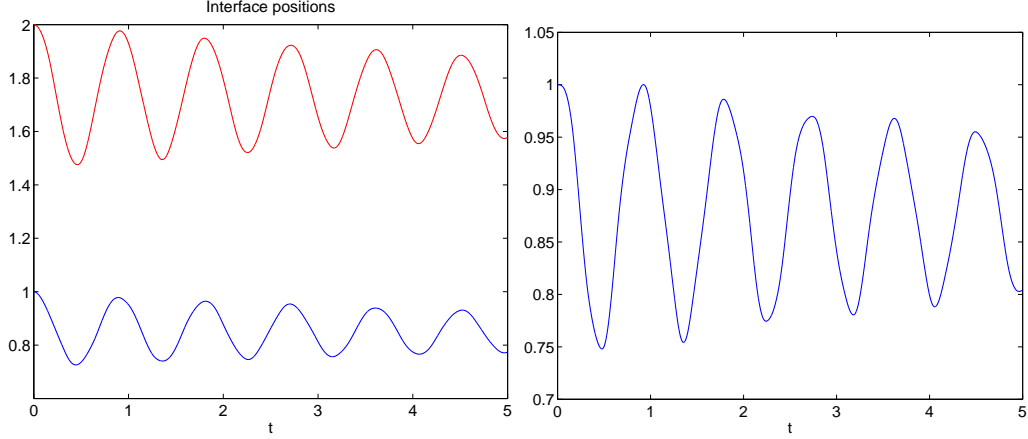


Figure 9: The position of the two fluid/solid interfaces as function of time (left). The length of the rod as function of time (right). 4/2 method. $h = 0.0125$.

8 shows the velocity for the same computation, and at the same times as the temperatures in Fig. 7. The movement of the object is illustrated by inspecting the magnitude and direction of the velocity. Fig. 9 gives another illustration of the bouncing character of the solution, by displaying the positions of the two interfaces as function of time. The figure shows how the dissipation mechanisms acts to reduce the amplitude with time. The right subfigure shows the length of the object, computed as the difference between the two positions in the left subfigure. The computations in Figs. 7–9 were all made with the 4/2 method on a grid with $h = 0.0125$.

Finally, we show in Fig. 10 the velocity at time 0.908 on grids of different resolutions. Figure 10 displays a close up of the solution near the lower fluid/structure interface. The three formal orders of accuracy 2, 4, and 6 (away from boundaries) are shown in Figs. 10a–c respectively. The reference solution, shown in black, was obtained with an extreme resolution, and verified to not change visibly in the plot under a factor two of grid refinement. The results with a coarser resolution of $h = 0.05$, shown in cyan/magenta (for fluid/structure), are compared with results obtained with the finer resolution $h = 0.025$, shown in blue/red (for fluid/structure). From Fig. 10 we infer that the higher order methods show considerably faster grid convergence than the second order method. The 6/3 method shows somewhat better convergence

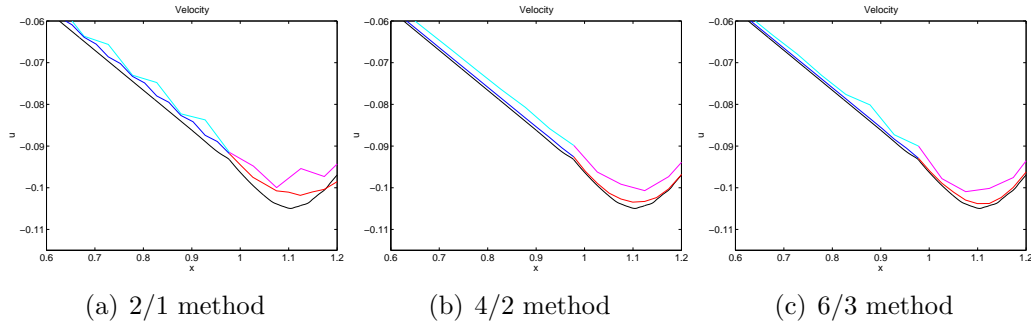


Figure 10: Grid convergence study. Close up view of the velocity at time 0.908 for $h = 0.05$ (fluid-cyan, solid-magenta), $h = 0.025$ (fluid-blue, solid-red). Reference solution shown in black.

than the 4/2 method, but as shown in Fig. 6, the difference would be more pronounced if the grids were refined further.

6 Conclusions

We have presented stable interface conditions for fluid/structure coupling in the context of high order accurate finite difference schemes. The method has been developed in a Lagrangian formulation for the equations of elasticity, with a moving grid for the Navier-Stokes equations that describes the fluid part of the computation. The interface conditions, which includes viscous effects and heat conduction, is proved to be linearly stable for semi-discrete approximations through norm estimates. Numerical experiments have shown the method to be stable with explicit time stepping up to the CFL limit given by the methods in the two subdomains. The interface conditions do not require any additional time step reduction.

We are currently generalizing the interface conditions to two and three space dimensions. If symmetrizers can be found for the multidimensional equations, the norm estimate technique presented here generalizes straightforwardly. The linearized three dimensional Navier-Stokes equations have known symmetrizers, see [1]. Symmetrizers for the system (1) are under investigation. The surface waves that occur along interfaces in more than one space dimension, are extra challenges for the multidimensional problem.

We have here only considered smoothly varying flow variables. However, there are many applications of fluid structure interaction where high speed flows with shock waves are of interest. Such flows can be computed by hybridizing the stable and accurate methods developed here with a more robust but less accurate shock capturing scheme. This is a well-known technique for computing compressible flows with both shock waves and small scale oscillatory behavior, see, e.g.,[12].

This work was performed under the auspices of the U.S. Department of Energy by Lawrence Livermore National Laboratory under Contract DE-AC52-07NA27344.

References

- [1] S. Abarbanel and D. Gottlieb. Optimal time splitting for two- and three-dimensional Navier-Stokes equations with mixed derivatives. *J. Comput. Phys.*, 41:1–33, 1981.
- [2] T. Belytschko, W. K. Liu, and B. Moran. *Nonlinear Finite Elements for Continua and Structures*. John Wiley & Sons Ltd., 2000.
- [3] M. H. Carpenter, D. Gottlieb, and S. Abarbanel. Time-stable boundary conditions for finite-difference schemes solving hyperbolic systems: Methodology and application to high-order compact schemes. *J. Comput. Phys.*, 111:220–236, 1994.
- [4] G. S. Chesshire and W. D. Henshaw. Composite overlapping meshes for the solution of partial differential equations. *J. Comput. Phys.*, 90(1):1–64, 1990.
- [5] L. Halpern. Artificial boundary conditions for incompletely parabolic perturbations of hyperbolic systems. *SIAM J. Math. Anal.*, 22:1256–1283, 1991.
- [6] W. D. Henshaw and K. K. Chand. A composite grid solver for conjugate heat transfer in fluid-structure systems. *J. Comput. Phys.*, 228:3708–3741, 2009.
- [7] J.W.Banks and B.Sjögreen. Stability of numerical interface conditions for fluid/structure interaction. *Commun. Comput. Phys.*, 10:279–304, 2011.

- [8] H.-O. Kreiss and N. A. Petersson. A second order accurate embedded boundary method for the wave equation with Dirichlet data. *SIAM J. Sci. Comput.*, 27:1141–1167, 2006.
- [9] H.-O. Kreiss, N. A. Petersson, and J. Yström. Difference approximations of the Neumann problem for the second order wave equation. *SIAM J. Numer. Anal.*, 42:1292–1323, 2004.
- [10] S. Nilsson, N. A. Petersson, B. Sjögreen, and H.-O. Kreiss. Stable finite difference approximations for the elastic wave equation in second order formulation. *SIAM J. Numer. Anal.*, 45:1902–1936, 2007.
- [11] P. Olsson. Summation by parts, projections, and stability. I. *Math. Comput.*, 64:1035–1065, 1995.
- [12] B. Sjögreen and H.C. Yee. Multiresolution wavelet based adaptive numerical dissipation control for shock-turbulence computation. *J. Sci. Comp.*, 20:211–255, 2004.
- [13] B. Strand. Summation by parts for finite difference approximations for d/dx . *J. Comput. Phys.*, 110:47–67, 1994.
- [14] M. L. Wilkins. *Computer simulation of dynamic phenomena*. Springer, 1999.